The Landau–Zener–Stückelberg–Majorana transition in the $T_2 \ll T_1$ limit

Michael C. Boucher[a], **Peter Sun**[a], **Ivan Keresztes**[a], **Lee E. Harrell**[b], **John A. Marohn**[a,*]

[a]Department of Chemistry and Chemical Biology, Cornell University, Ithaca, New York 14853, USA

[b]Department of Physics and Nuclear Engineering, U.S. Military Academy, West Point, New York 10996, USA

Abstract

Landau–Zener–Stückelberg–Majorana (LZSM) transitions occur between quantum states when parameters in the system's Hamiltonian are varied continuously and rapidly. In magnetic resonance, losses in adiabatic rapid passage can be understood using the physics of LZSM transitions. Most treatments of LZSM transitions ignore the T_2 dephasing of coherences, however. Motivated by ongoing work in magnetic resonance force microscopy, we employ the Bloch equations, coordinate transformation, and the Magnus expansion to derive expressions for the final magnetization following a rapid field sweep at fixed irradiation intensity that include T_2 losses. Our derivation introduces an inversion-function, Fourier transform method for numerically evaluating highly oscillatory integrals. Expressions for the final magnetization are given for low and high irradiation intensity, valid in the $T_2 \ll T_1$ limit. Analytical results are compared to numerical simulations and nuclear magnetic resonance experiments. Our relatively straightforward calculation reproduces semiquantitatively the well known LZSM result in the $T_2 \to 0$ limit.

Graphical Abstract
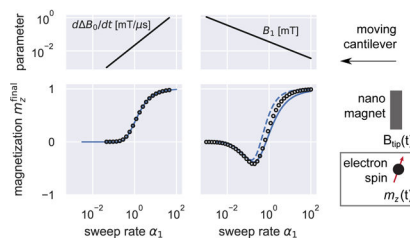
*Corresponding author: jam99@cornell.edu (John A. Marohn).

Supplementary material
Longitudinal relaxation time data and fits (peak integral vs. time, Fig. S1); transverse relaxation time data and fits (peak integral vs. time, Fig. S2); and additional measurements of final magnetization after a sweep through resonance, carried out at different sweep rates and sweep times (Figs. S3 and S4).

Keywords

Landau–Zener–Stückelberg–Majorana transition; Landau–Zener transition; Bloch equations; electron spin resonance; saturation; adiabatic rapid passage; magnetic resonance force microscopy; force-gradient detected magnetic resonance

1. Introduction

The rapid detection and imaging of single electron spins would be a powerful tool for the atomic-scale characterization of samples ranging from emerging quantum computing materials to individual spin-labeled biomolecules. Applying single-spin imaging to nitroxide spin labels — widely employed to study globular proteins, membrane proteins, and nucleic acids — is an especially exciting prospect. Since pioneering experiments in the early 1990's optically detected magnetic resonance in individual pentacene molecules [1, 2], more widely applicable magnetic resonance experiments have demonstrated the detection and imaging of individual electron spins. The two most generally applicable such experiments involve using magnetic resonance force microscopy to detect an individual E′ defect in quartz [3] and employing a nitrogen-vacancy center in diamond to observe a single adventitious radical located nearby [4, 5].

Frustratingly, both these experiments observed essentially unpolarized spins and consequently required signal-averaging times of 13 hour/pt. in Ref. 3 and 40 min/pt. in Ref. 5 [6]. For imaging nitroxide-labeled proteins, magnetic resonance force microscopy (MRFM) is preferable to NV-center magnetometry because of the MRFM experiment's superior depth of view. Moore and coworkers showed that small numbers of nitroxide spins could be observed as a cantilever frequency shift in an MRFM experiment [7]. Motivated by this breakthrough, Nguyen and Marohn proposed a single-spin MRFM experiment optimized to detect and image individual nitroxide spin labels using a magnet-tipped cantilever, with an estimated signal averaging time of only seconds per point [8]. In contrast with the spin-noise experiments of Refs. 3 and 5, the proposed experiment measures the average (*i.e.* thermal) spin polarization, greatly improving the signal-averaging statistics.

In the Ref. 8 proposal, spin magnetization is manipulated with short bursts of microwave irradiation applied in synchrony with cantilever motion. The resulting changes in spin magnetization are detected as a force-gradient-induced shift in cantilever frequency [7, 9]. Computing spin evolution in the Ref. 8 experiment is challenging. To detect spin-induced changes in cantilever frequency, the cantilever must be moving. Large time-dependent resonance offsets are experienced by electron spins below the moving magnet-tipped cantilever, and one is concerned that the resonance offset changes so rapidly that spins may not be in resonance with the applied microwaves long enough to invert or even saturate. The purpose of this manuscript is to assess the potential loss of signal due to this effect.

The magnetic resonance community is familiar with the problem of magnetization loss during an adiabatic rapid passage through resonance [10–18]. Adiabatic rapid passage is an example of a Landau–Zener–Stückelberg–Majorana (LZSM) transition [19] — wavefunction evolution that occurs when the Hamiltonian parameters are changed

continuously. LZSM transitions are used to describe a wide range of phenomena beyond magnetic resonance — atomic collisions [20] chemical reaction rates [21, 22], population inversion in electronic states [23], and qubit control [24–27] for example. LZSM transitions have recently been used to describe the quantum dynamics of two coupled qubits [28, 29], qutrits [30–32], coupled qutrits [29], and quantum annealing protocols [33].

State-to-state transition probabilities following an LZSM transition can be calculated for a two-level system exactly using the Schrödinger equation [19, 26, 27, 34]. If the frequency of applied irradiation is swept through resonance too quickly, level populations are unaffected by the irradiation. If, on the other hand, the irradiation is swept through resonance slowly, *i.e. adiabatically*, then a population inversion is achieved. The Schrödinger-equation treatment of the LZSM transition is not obviously valid at low irradiation intensity and, moreover, neglects relaxation. Our nitroxide spin of interest has $T_2 = 0.45 \ \mu s$, comparable to or shorter than the time to sweep through resonance in a magnetic resonance force microscope experiment. Relaxation during a rapid passage through resonance is, therefore, a concern.

Assessing how relaxation modifies the transition probabilities during an LZSM transition is an area of active research. There are two issues to consider in magnetic resonance versions of the LZSM experiment. The first is computing spin relaxation during a perfectly adiabatic sweep through resonance; even when losses due to violation of the adiabatic condition are negligible, magnetization can still be lost due to relaxation. There is a large body of magnetic resonance literature treating relaxation from dipolar interactions and chemical exchange during an adiabatic, frequency-swept pulse [35–42]. This body of literature, however, neglects non-adiabatic losses.

The second issue is computing the final magnetization when the adiabatic condition is violated *and* relaxation is present. This is the issue considered here. One must take care assessing LZSM-transition studies, because, outside the magnetic resonance literature, non-adiabatic losses are often called "dissipation" despite their being due to neither T_1 nor T_2 relaxation. While numerous studies have modeled T_2 losses during an LZSM transition [23, 43–55], none of these studies obtain a simple and accurate closed-form solution for the T_2-modified transition probabilities in the simple case of a linear energy-level sweep, and none consider both low- and high-intensity irradiation.

To address this deficiency, here we compute the magnetization evolution following a fast sweep through resonance in the $T_2 \ll T_1$ limit using the Bloch equations [56–59], coordinate transformations, and the Magnus expansion [60, 61]. We consider both low-intensity and high-intensity limits and obtain approximate solutions for the magnetization following an LZSM transition that accounts for T_2 losses.

2. Theory

2.1. The connection between LZSM transitions and the Bloch equations

To see the connection between LZSM transitions and the Bloch equations, let us write out the LZSM problem in the language of magnetic resonance. Consider a spin with magnetic

moment $\boldsymbol{\mu} = \hbar\gamma\boldsymbol{I}$, with $\hbar$ Planck's constant, γ the spins's gyromagnetic ratio, and $\boldsymbol{I}$ the unitless angular momentum operator having components I_x, I_y, and I_z. This spin is placed in a magnetic field $\boldsymbol{B}(t) = B_0(t)\hat{z} + B_1(\cos(\omega t)\hat{\boldsymbol{x}} + \sin(\omega t)\hat{\boldsymbol{y}})$, formed from a longitudinal magnetic field of magnitude $B_0(t)$ plus a transverse magnetic field of magnitude B_1 rotating about the $\hat{z}$ axis at angular frequency ω. The Hamiltonian for the spin, $\mathscr{H} = -\boldsymbol{\mu} \cdot \boldsymbol{B}$, is given by

$$\mathscr{H}(t) = \hbar\omega_0(t)I_z + \hbar\omega_1(\cos(\omega t)I_x + \sin(\omega t)I_y).$$

(1)

with $\omega_0(t) = -\gamma B_0(t)$ the (time-dependent) Larmor frequency and $\omega_1 = -\gamma B_1$ the Rabi frequency. The eq. 1 Hamiltonian gives rise to LZSM transitions, instead of the usual Rabi oscillations, because in eq. 1 the longitudinal field amplitude $B_0(t)$ is now time-dependent; a static field B_0 and time-dependent irradiation frequency $\omega(t)$ also yields LSZM transitions.

Consider the resulting dynamics of a spin $I = 1/2$ particle having two energy levels: a ground state and an excited state. In the eigenbasis of the I_z operator, the spin's wavefunction is given by

$$\psi(t) = \begin{pmatrix} c_e(t) \\ c_g(t) \end{pmatrix}$$

(2)

with $c_g(t)$ and $c_e(t)$ the ground-state and excited-state wavefunction coefficients, respectively. Plugging $\psi(t)$ and $\mathscr{H}(t)$ into the Schrödinger equation gives a set of two coupled non-linear equations for $c_g(t)$ and $c_e(t)$. These coupled equations can be simplified by applying a unitary, rotating-frame transformation $\widetilde{\psi} = U\psi$ with $U = e^{i\omega t I_z}$. The transformed wavefunction is governed by an effective Hamiltonian $\mathscr{H}_{\text{eff}} = U\mathscr{H}U^{\dagger} + i\dot{U}U^{\dagger} = (\omega_0(t) - \omega)I_z + \omega_1 I_x$, leading to the following two coupled differential equations for the complex-valued coefficients of the wavefunction $\widetilde{\psi}$

$$i\dot{\tilde{c}}_e = \frac{1}{2}(\omega_0(t) - \omega)\tilde{c}_e + \frac{1}{2}\omega_1\tilde{c}_g$$

(3)

$$i\dot{\tilde{c}}_g = \frac{1}{2}\omega_1\tilde{c}_e - \frac{1}{2}(\omega_0(t) - \omega)\tilde{c}_g.$$

(4)

Eliminating $\tilde{c}_g$ gives a second order differential equation for $\tilde{c}_e(t)$. For a linear sweep through resonance, $\omega_0(t) - \omega = -vt$ and the coefficients in this differential equation are time dependent. Closed-form solutions for $\tilde{c}_e(t \to \infty)$ and $\tilde{c}_g(t \to \infty)$, given $c_e(0)$ and $c_g(0)$, can be written in terms of Weber functions [19].

According to the Feynman-Vernon-Hellwarth theorem [58], the dynamics of a two-level quantum system can be solved by following the time evolution of a real, three-dimensional vector whose components are

$$u = \tilde{c}_e\tilde{c}_g^* + \tilde{c}_g\tilde{c}_e^*$$

(5)

$$v = i\left(\tilde{c}_e\tilde{c}_g^* - \tilde{c}_g\tilde{c}_e^*\right)$$

(6)

$$w = \tilde{c}_e\tilde{c}_e^* - \tilde{c}_g\tilde{c}_g^*.$$

(7)

For the magnetic two-level system, the numbers u, v, and w are the components of the Bloch unit vector that points in the direction of spin's magnetization. Recasting the LZSM problem in terms of the Bloch vector, we obtain the Bloch equations of the next section in the $T_1 \to \infty$ and $T_2 \to \infty$ limit. By recasting the LZSM problem as a modified set of Bloch equations, we can introduce saturation and dephasing effects by adding finite T_1 and T_2.

2.2. Unitless Bloch equations

Defining a unitless magnetization vector as follows,

$$\boldsymbol{m} = (u, v, w)^T = \frac{1}{M_{eq}}(M_x, M_y, M_z)^T,$$

(8)

with M_{eq} the thermal-equilibrium magnetization, the Bloch equations in the rotating frame can be written as

$$\frac{d}{d\tau}\begin{pmatrix} u \\ v \\ w \end{pmatrix} = \underbrace{\begin{pmatrix} -\beta & \delta & 0 \\ -\delta & -\beta & 1 \\ 0 & -1 & -\alpha \end{pmatrix}}_{\text{Bloch matrix } \boldsymbol{B}} \begin{pmatrix} u \\ v \\ w \end{pmatrix} + \underbrace{\begin{pmatrix} 0 \\ 0 \\ \alpha \end{pmatrix}}_{\text{vector } \boldsymbol{b}}$$

(9)

with

$$\tau \equiv \gamma B_1 t$$

(10)

a unitless time parameter created by multiplying time t by the Rabi frequency γB_1, with γ the electron gyromagnetic ratio and B_1 the irradiation intensity in the rotating frame. The

inverse Rabi frequency is chosen as the time basis because B_1 is held constant in experiments considered here. In eq. 9

$$\alpha \equiv \frac{1}{\gamma B_1 T_1}$$

(11)

and

$$\beta \equiv \frac{1}{\gamma B_1 T_2}$$

(12)

are unitless relaxation-time parameters and

$$\delta \equiv \Delta B_0 / B_1$$

(13)

is a unitless resonance-offset parameter, with $\Delta B_0 = B_0 - \omega/\gamma$ the resonance offset and ω the irradiation frequency. In experiments considered here, ω is constant, and B_0 is time-dependent due to tip motion in the MRFM experiment.

If we neglect the relaxation terms in the Bloch matrix, then eq. 9 is equivalent to $\dot{\boldsymbol{m}} = \boldsymbol{m} \times \boldsymbol{b}_{\text{eff}}$ with $\boldsymbol{b}_{\text{eff}} = \hat{\boldsymbol{x}}_r + \delta\hat{z}$ an effective magnetic field in the rotating frame and $\hat{\boldsymbol{x}}_r$, $\hat{\boldsymbol{y}}_r$, and $\hat{z}$ the rotating-frame unit vectors. The above $\dot{\boldsymbol{m}}$ equation describes the undamped precession of magnetization about the effective field in the rotating frame.

2.3. Breakdown of saturation when the resonance offset is time-dependent

Closed-form solutions to eq. 9 can be obtained when the intensity, B_1, and resonance offset, ΔB_0, of the applied irradiation are both time-independent. In the presence of the moving tip in the MRFM experiment, however, spins experience a large time-dependent resonance offset. The evolution of magnetization in this situation requires the development of approximate solutions. Below we develop approximate solutions in a low-B_1 limit and a high-B_1 limit. The transition between the two limits occurs at a critical field

$$B_1^{\text{crit}} = \frac{1}{2\gamma}\left(\frac{1}{T_2} - \frac{1}{T_1}\right)$$

(14)

below which all the Bloch-matrix eigenvalues are real, and no Rabi oscillations are evident.

2.4. Breakdown in the low-B_1 limit

We are interested in spins with $T_2 \ll T_1$, *i.e.* $\beta \gg \alpha$. In this limit, the transverse magnetization quickly reaches a pseudo-equilibrium with the slowly evolving longitudinal magnetization.

We can use this pseudo-equilibrium condition to develop a useful approximation for how the rate at which the longitudinal magnetization reaches equilibrium depends on irradiation intensity and resonance offset.

The Bloch equations describing the unitless transverse magnetization can be written

$$\frac{d}{d\tau}\begin{pmatrix} u \\ v \end{pmatrix} = \begin{pmatrix} -\beta & \delta \\ -\delta & -\beta \end{pmatrix}\begin{pmatrix} u \\ v \end{pmatrix} + \begin{pmatrix} 0 \\ w(\tau) \end{pmatrix}$$

(15)

where we write $w(\tau)$ to emphasize that the z-axis magnetization is time dependent. Let us nevertheless treat $w(\tau)$ in the above equation as if it was time-independent and solve for the steady-state transverse magnetization. The result is

$$u_{ss} = \frac{\delta}{\beta^2 + \delta^2} w(\tau) \text{ and } v_{ss} = \frac{\beta}{\beta^2 + \delta^2} w(\tau).$$

(16)

We should regard $w(\tau)$ in these equations as a slowly varying function of time that u and v respond to instantaneously. Substituting $u \to u_{ss}$ in the Bloch equation for w, we obtain the differential equation

$$\frac{d}{d\tau} w = -\underbrace{\left(\alpha + \frac{\beta}{\beta^2 + \delta(\tau)^2} \right)}_{r_{eff}(\tau)} w + \alpha$$

(17)

where the underbraced term is an effective relaxation rate $r_{eff}(\tau)$. This rate is time-dependent if the resonance offset is time-dependent, as indicated. Changing the independent variable in eq. 17 from τ to t we obtain a new differential equation $dw/dt = -r_{eff}(t)w + T_1^{-1}$, with

$$r_{eff}(t) = \frac{1}{T_1} + \frac{(\gamma B_1)^2 T_2}{1 + (\gamma T_2 \Delta B_0(t))^2}$$

(18)

the effective relaxation rate in units of s^{-1}, now written in terms of time t. The above treatment is valid when $r(t) \ll 1/T_2$, which is true, assuming $T_2 \ll T_1$, when $B_1 \ll B_{homog}$ with

$$B_{homog} = \frac{1}{\gamma T_2}$$

(19)

the homogeneous linewidth. In other words, the solution is valid in the low-B_1 limit.

Now consider an experiment in which the resonance offset is swept from above resonance (at time $-t_0$) to below resonance (at time t_0). In this experiment, the unitless resonance offset can be expressed as follows

$$\delta(\tau) = -\alpha_1 \pi \tau$$

(20)

with

$$\alpha_1 \equiv \frac{1}{\pi \gamma B_1^2} \frac{d\Delta B_0}{dt}$$

(21)

a unitless sweep-rate parameter. We are interested in the z-magnetization at the end of the sweep. The exact solution to eq. 17 is

$$w(\tau_0) = e^{-R(\tau_0)} w(-\tau_0) + \alpha e^{-R(\tau_0)} \int_{-\tau_0}^{\tau_0} e^{R(\tau)} d\tau$$

(22)

with $\tau_0 = \gamma B_1 t_0$,

$$R(\tau_0) = \int_{-\tau_0}^{\tau_0} r_{\text{eff}}(\tau') d\tau' = \alpha \tau_0 + \frac{2 \arctan{(a_0/\beta)}}{\pi \alpha_1},$$

(23)

and $a_0 = \pi \alpha_1 \tau_0$. The argument of the arctan function in the above equation can be written

$$\frac{a_0}{\beta} = \gamma T_2 t_0 \frac{d\Delta B_0}{dt} = \frac{B_{\text{final}}}{B_{\text{homog}}}$$

(24)

with $B_{\text{final}} = t_0 d\Delta B_0/dt$ the resonance offset at the end of the sweep.

In the limit that (a) $B_{\text{final}} \gg B_{\text{homog}}$ and (b) the sweep time $2t_0$ is fast compared to T_1 (*i.e.* $\alpha \tau_0 \ll 1$), the integrated relaxation rate simplifies to $R(\tau_0) \approx 1/\alpha_1$. Making these assumptions, and switching notation $w \to m_z$ for clarity, the second term in eq. 22 can be neglected and

$$m_z^{\text{final}} = e^{-1/\alpha_1} m_z^{\text{initial}}$$

(25)

in the low-B_1 limit. When the field is swept slowly through resonance, $\alpha_1 \ll 1$, the final z magnetization is zero, and the sample has been fully saturated. On the other hand, when

the field is swept quickly through resonance, $\alpha_1 \gg 1$, $m_z^{\text{final}} \approx m_z^{\text{initial}}$, and the magnetization is essentially unaffected by the irradiation.

2.5. Breakdown in the high-B_1 limit

For sufficiently high B_1 and sufficiently slow sweep rate, when δ is swept from well above resonance to well below resonance, the magnetization m follows the effective field b_{eff} adiabatically. The initial unitless magnetization is $m^{\text{init}} = (0, 0, 1)^T$. Ideally, if B_1 is suitably strong and the sweep suitably slow, then the final magnetization is $(0, 0, -1)^T$. If these conditions are not met, then m_z^{final} will deviate from -1.

Klein *et al.* [62] and Harrell *et al.* [63] have considered the loss of magnetization during adiabatic rapid passage in the context of magnetic resonance force microscope experiments. Following Harrell *et al.*, the probability of a deleterious diabatic transition follows from the long-known LZSM result [34, 64],

$$P_{\text{dia}} = e^{-1/2\alpha_1}$$

(26)

with α_1 the unitless sweep-rate parameter given by eq. 21 above. We see that this parameter also governs the efficacy of the adiabatic rapid passage. The probability of *not* making a diabatic transition is

$$P_{\text{adia}} = 1 - P_{\text{dia}} = 1 - e^{-1/2\alpha_1}.$$

(27)

Assume the initial magnetization is $m^{\text{init}} = (0, 0, 1)^T$. If the magnetization follows the effective field adiabatically, then final z-component of magnetization is $m_z^{\text{final}} = -1$. If, on the other hand, a diabatic transition occurs, then the magnetization remains unchanged by the sweep and $m_z^{\text{final}} = 1$. To obtain the final magnetization, we should weight each of these two possible outcomes by their probabilities,

$$m_z^{\text{final}} = -1 P_{\text{adia}} + 1 P_{\text{dia}}$$

(28)

$$= -1 + 2e^{-1/2\alpha_1}.$$

(29)

The adiabatic rapid passage is successful, $m_z^{\text{final}} \approx -1$, when $\alpha_1 \ll 1$ (*i.e.* B_1 is large and dB_0/dt is small).

While the LZSM result is a remarkably simple equation, the result comes from a limiting solution to the Schrödinger equation, so completely neglects relaxation. Our sample of

interest has a short T_2, so we are concerned about the validity of neglecting relaxation. We now use the Bloch equations to derive a result analogous to eq. 29. This approach opens a route to amending the Landau-Zener result to capture additional losses of magnetization due to T_2 relaxation during the rapid passage through resonance.

To describe the loss of magnetization during a rapid passage through resonance, let us first approximate eq. 9 by neglecting the inhomogeneous term,

$$\dot{\boldsymbol{m}} \approx \boldsymbol{Bm}$$

(30)

With the resonance offset time-dependent, $\delta(t)$, let us work in a tilted coordinate system that keeps the effective field directed along the z axis. We define a tilted magnetization $\boldsymbol{m}_a$ as follows

$$\boldsymbol{m} = \boldsymbol{T}_a \boldsymbol{m}_a$$

(31)

with $\boldsymbol{T}_a$ a coordinate-rotation matrix. The inverse relation is $\boldsymbol{m}_a = \boldsymbol{T}_a^{-1}\boldsymbol{m}$. Plugging eq. 31 into 30 we obtain the following differential equation governing the evolution of the rotated magnetization,

$$\dot{\boldsymbol{m}}_a = \underbrace{\left(\boldsymbol{T}_a^{-1}\boldsymbol{B}\boldsymbol{T}_a - \boldsymbol{T}_a^{-1}\dot{\boldsymbol{T}}_a\right)}_{\text{effective Bloch matrix } \boldsymbol{B}_{\text{eff}}^a} \boldsymbol{m}_a$$

(32)

Using the intuition that tilting the rotating-frame around the $\hat{\boldsymbol{y}}_r$ axis will align $\boldsymbol{b}_{\text{eff}}$ with the $\hat{z}$ axis, we choose $\boldsymbol{T}_a$ to be a rotation around the $\hat{\boldsymbol{y}}_r$ axis:

$$\boldsymbol{T}_a = \boldsymbol{R}_y(\theta) = \begin{pmatrix} \cos\theta & 0 & \sin\theta \\ 0 & 1 & 0 \\ -\sin\theta & 0 & \cos\theta \end{pmatrix}$$

(33)

with

$$\theta(\tau) = \begin{cases} \tan^{-1}(1/\delta(\tau)) & \delta(\tau) \geq 0 \\ \tan^{-1}(1/\delta(\tau)) + \pi & \delta(\tau) < 0. \end{cases}$$

(34)

At large positive resonance offset, θ is zero, $\boldsymbol{T}_a$ is the diagonal matrix, and the axes are untilted. At large negative resonance offset, $\boldsymbol{T}_a$ implements a 180° rotation around the $\hat{\boldsymbol{y}}_r$ axis.

Using trigonometric relations,

$$\sin\theta(\tau) = \frac{1}{\sqrt{1 + \delta(\tau)^2}}$$

(35)

$$\cos\theta(\tau) = \frac{\delta(\tau)}{\sqrt{1 + \delta(\tau)^2}}.$$

(36)

Substituting Eqs. 33 through 36 into eq. 32 yields the following effective Bloch matrix in the tilted frame

$$\boldsymbol{B}_{\text{eff}}^a = \begin{pmatrix} -\dfrac{\alpha + \beta\delta^2}{1 + \delta^2} & \sqrt{1 + \delta^2} & \dfrac{(\alpha - \beta) + \dot{\delta}}{1 + \delta^2} \\ -\sqrt{1 + \delta^2} & -\beta & 0 \\ \dfrac{(\alpha - \beta) - \dot{\delta}}{1 + \delta^2} & 0 & -\dfrac{\beta + \alpha\delta^2}{1 + \delta^2} \end{pmatrix}.$$

(37)

For compactness, we have dropped the explicit time dependence of δ. Neglecting relaxation by setting $\alpha \to 0$ and $\beta \to 0$ gives the approximate Bloch matrix

$$\boldsymbol{B}_{\text{eff}}^a \approx \begin{pmatrix} 0 & \sqrt{1 + \delta^2} & \dfrac{\dot{\delta}}{1 + \delta^2} \\ -\sqrt{1 + \delta^2} & 0 & 0 \\ -\dfrac{\dot{\delta}}{1 + \delta^2} & 0 & 0 \end{pmatrix}.$$

(38)

This Bloch matrix describes the precession of magnetization about an effective field

$$\boldsymbol{b}_{\text{eff}}^a = \sqrt{1 + \delta^2}\,\hat{z}_a + \frac{\dot{\delta}}{1 + \delta^2}\,\hat{\boldsymbol{y}}_a$$

(39)

with $\hat{z}_a$ and $\hat{\boldsymbol{y}}_a$ unit vectors in the tilted frame of reference defined by $\boldsymbol{T}_a$. Because δ is time dependent, the direction of $\boldsymbol{b}_{\text{eff}}^a$ is continuously changing, giving rise to complicated magnetization dynamics, even in the tilted frame of reference.

To simplify the evolution further, let us apply an additional rotation to our coordinate system. Let the magnetization in the new coordinate system be

$$\boldsymbol{m}_a = \boldsymbol{T}_b \boldsymbol{m}_b$$

(40)

with

$$\boldsymbol{T}_b = \boldsymbol{R}_z(\phi(\tau)) = \begin{pmatrix} \cos\phi(\tau) & -\sin\phi(\tau) & 0 \\ \sin\phi(\tau) & \cos\phi(\tau) & 0 \\ 0 & 0 & 1 \end{pmatrix}$$

(41)

a transformation designed to rotate the magnetization $\boldsymbol{m}_a$ around $\hat{z}_a$, the $\hat{z}$ axis in the tilted frame; below we will choose $\phi(\tau)$ judiciously to simplify the effective Bloch matrix. The rotated magnetization $\boldsymbol{m}_b$ is now governed by the differential equation

$$\dot{\boldsymbol{m}}_b = \boldsymbol{B}_{\text{eff}}^b \boldsymbol{m}_b$$

(42)

where the effective Bloch matrix is given by

$$\boldsymbol{B}_{\text{eff}}^b(\tau) = \boldsymbol{T}_b^{-1} \boldsymbol{B}_{\text{eff}}^a \boldsymbol{T}_b - \boldsymbol{T}_b^{-1} \dot{\boldsymbol{T}}_b$$

(43)

which reduces to

$$\begin{pmatrix} 0 & \sqrt{1 + \delta(\tau)^2} + \dot{\phi}(\tau) & \frac{\cos\phi(\tau)\dot{\delta}(\tau)}{1 + \delta(\tau)^2} \\ -\sqrt{1 + \delta(\tau)^2} - \dot{\phi}(\tau) & 0 & \frac{\sin\phi(\tau)\delta(\tau)}{1 + \delta(\tau)^2} \\ -\frac{\cos\phi(\tau)\dot{\delta}(\tau)}{1 + \delta(\tau)^2} & -\frac{\sin\phi(\tau)\dot{\delta}(\tau)}{1 + \delta(\tau)^2} & 0 \end{pmatrix}.$$

(44)

For a linear field sweep, evolving from way above resonance to way below, $\delta(\tau)$ is given by eq. 20. Here we have used eqs. 10, 13, and 21 to write the time-dependent resonance offset in unitless form.

We are interested in following magnetization from time $-\tau_0$ to $+\tau_0$ where we will ultimately take the limit $\tau_0 \to \infty$. The effective Bloch matrix $\boldsymbol{B}_{\text{eff}}^b(\tau)$ can be simplified by choosing the phase angle $\phi(\tau)$ to be

$$\phi(\tau) = \phi_0 + \int_{-\tau_0}^{\tau} d\tau' \sqrt{1 + \delta(\tau')^2}.$$

(45)

This choice of phase makes the (1,2) and (2,1) matrix elements of $\boldsymbol{B}_{\text{eff}}^{b}(\tau)$ vanish. Carrying out the above integral,

$$\phi(\tau) = \frac{1}{2}\tau\sqrt{1 + \alpha_1^2 \pi^2 \tau^2} + \frac{1}{2\pi\alpha_1}\operatorname{arcsinh}(\pi\alpha_1\tau)$$

(46)

where, for simplicity, we have set the initial condition to be

$$\phi_0 = -\frac{1}{2}\tau_0\sqrt{1 + \alpha_1^2 \pi^2 \tau_0^2} - \frac{1}{2\pi\alpha_1}\operatorname{arcsinh}(\pi\alpha_1\tau_0).$$

(47)

Choosing this initial phase is required to obtain a phase of $\phi = 0$ at $\tau = 0$, when the system has reached resonance.

To solve eq. 42 we use a 1$^{\text{st}}$-order Magnus expansion [60, 61]. We are interested in the long-time solution, so will take the integration limits to be $-\infty$ and $+\infty$. In integrating eq. 44 to obtain the 1$^{\text{st}}$-order Magnus exponent Ω_1 below we used a change of variables $a = \pi\alpha_1\tau$; the variable $a_0 = \pi\alpha_1\tau_0$ is the associated integration limit. We obtain

$$\boldsymbol{m}_b(+\infty) \approx e^{\Omega_1}\boldsymbol{m}_b(-\infty)$$

(48)

with

$$\Omega_1 = \int_{-\infty}^{+\infty}\boldsymbol{B}_{\text{eff}}^{b}(\tau)d\tau = \begin{pmatrix} 0 & 0 & -\pi I_{13}(t_{\text{sweep}}) \\ 0 & 0 & 0 \\ \pi I_{13}(t_{\text{sweep}}) & 0 & 0 \end{pmatrix}$$

(49)

where the relevant integral can be written as follows

$$I_{13}(a_0, t_{\text{sweep}}) = \int_{-a_0}^{+a_0}\frac{1}{\pi}\frac{\cos(2\pi t_{\text{sweep}}g(a))}{1 + a^2}da$$

(50)

with

$$t_{\text{sweep}} = \frac{1}{(2\pi)^2 \alpha_1}$$

(51)

a unitless sweep-time parameter, and

$$g(a) = a\sqrt{1 + a^2} + \text{arcsinh}(a).$$

(52)

In writing eq. 49 we have employed the convention that when the integral I_{13} is written with a single argument, the integration limits are assumed to be $(-\infty, +\infty)$, *i.e.* $I_{13}(t_{\text{sweep}}) = I_{13}(\infty, t_{\text{sweep}})$. In writing eq. 49 we have also used that the $\sin(\phi(\tau))$ integral vanishes by symmetry.

By inspection, $I_{13}(t_{\text{sweep}})$ runs from 1 to 0 as the inverse-sweep-rate parameter t_{sweep} runs from 0 to ∞. However, the eq. 50 integrand is highly oscillatory, and $I_{13}(t_{\text{sweep}})$ is therefore challenging to compute both quickly and accurately at arbitrary t_{sweep}. A fast numerical method for computing the eq. 50 integral is reported in Appendix A. The integral I_{13} is plotted versus the parameter t_{sweep} in Fig. A.8.

Taking into account eqs. 48 and 49 and eq. 31, the final magnetization in the rotating frame is given by

$$m_z^{\text{final}} = -\cos(\pi I_{13}(t_{\text{sweep}}))m_z^{\text{initial}}$$

(53)

with t_{sweep} given by eq. 51. The final magnetization $\boldsymbol{m}_z^{\text{final}}$ is plotted versus the unitless sweep-rate α_1 in Fig. 1. The LZSM result, eq. 29, is plotted for comparison. We can see in Fig. 1 that eq. 53 predicts semiquantitatively the LZSM breakdown of adiabatic rapid passage through resonance at high α_1.

In summary, neglecting relaxation, we can recover Landau–Zener–Stückelberg–Majorana behavior from the Bloch equations using appropriately chosen coordinate transformations and the Magnus expansion.

We now expand our treatment to include T_2-related magnetization losses during rapid passage. Returning to eq. 37, we set $\alpha \to 0$, retain β, and recompute $\boldsymbol{B}_{\text{eff}}^b$, eq. 44, setting the angle $\phi(\tau)$ according to eq. 45. The result is

$$\boldsymbol{B}_{\text{eff}}^b(\tau) = \begin{pmatrix} -\beta + \beta\dfrac{\cos^2\phi(\tau)}{1 + \delta(\tau)^2} & \dfrac{\beta}{2}\dfrac{\sin 2\phi(\tau)}{1 + \delta(\tau)^2} & \dfrac{\cos\phi(\tau)\left(-\beta\delta(\tau) + \dot{\delta}(\tau)\right)}{1 + \delta(\tau)^2} \\[2ex] \dfrac{\beta}{2}\dfrac{\sin 2\phi(\tau)}{1 + \delta(\tau)^2} & -\dfrac{\beta}{2}\dfrac{1 + \cos 2\phi(\tau) + 2\delta(\tau)^2}{1 + \delta(\tau)^2} & \dfrac{\sin\phi(\tau)\left(-\beta\delta(\tau) + \dot{\delta}(\tau)\right)}{1 + \delta(\tau)^2} \\[2ex] -\dfrac{\cos\phi(\tau)\left(\beta\delta(\tau) + \dot{\delta}(\tau)\right)}{1 + \delta(\tau)^2} & -\dfrac{\sin\phi(\tau)\left(\beta\delta(\tau) + \dot{\delta}(\tau)\right)}{1 + \delta(\tau)^2} & -\dfrac{\beta}{1 + \delta(\tau)^2} \end{pmatrix}.$$

(54)

Integrating $\boldsymbol{B}_{\mathrm{eff}}^{b}(\tau)$ over $(-\infty, +\infty)$ to obtain the first-order Magnus exponent Ω_1 is now problematic, giving a divergent answer. To avoid this divergence, let us instead compute Ω_1 by integrating from $(-\tau_0, +\tau_0)$ as follows:

$$\Omega_1(\tau_0) = \int_{-\tau_0}^{+\tau_0} \boldsymbol{B}_{\mathrm{eff}}^{b}(\tau) d\tau$$

(55)

with

$$\Omega_1(\tau_0) = \begin{pmatrix} -2\beta\tau_0 + \dfrac{I_1(a_0) + I_{11}(a_0, t_{\mathrm{sweep}})}{2\alpha_2} & 0 & -\pi I_{13}(a_0, t_{\mathrm{sweep}}) \\ 0 & -2\beta\tau_0 + \dfrac{I_1(a_0) - I_{11}(a_0, t_{\mathrm{sweep}})}{2\alpha_2} & \dfrac{I_{23}(a_0, t_{\mathrm{sweep}})}{\alpha_2} \\ +\pi I_{13}(a_0, t_{\mathrm{sweep}}) & \dfrac{I_{23}(a_0, t_{\mathrm{sweep}})}{\alpha_2} & -\dfrac{I_1(a_0)}{\alpha_2} \end{pmatrix}.$$

(56)

In the above equation, the integration limit is $a_0 = \pi\alpha_1\tau_0$. The new integrals appearing in Ω_1 are $I_1(a_0) = 2\arctan(a_0)/\pi$, $I_{11}(a_0, t_{\mathrm{sweep}}) = I_{13}(a_0, 2t_{\mathrm{sweep}})$, and

$$I_{23}(a_0, t_{\mathrm{sweep}}) = \int_{-a_0}^{+a_0} \frac{1}{\pi} \frac{a \sin(2\pi t_{\mathrm{sweep}} g(a))}{1 + a^2} da.$$

(57)

The integrals I_{11} and I_{23} are plotted versus the inverse sweep-rate parameter $t_{\mathrm{sweep}} = 1/(2\pi)^2\alpha_1$ in Fig. A.8. Also appearing in Ω_1 is a second unitless sweep-rate parameter

$$\alpha_2 \equiv \frac{T_2}{\pi B_1} \frac{d\Delta B_0}{dt}.$$

(58)

We can see that eq. 49 is recovered from eq. 56 by taking the $T_2 \to \infty$ limit (*i.e.* setting $\beta \to 0$ and $\alpha_2 \to \infty$). Comparing eqs. 21 and 58,

$$\alpha_2 = \frac{B_1}{B_{\mathrm{homog}}}\alpha_1,$$

(59)

where $B_{\mathrm{homog}} = 1/\gamma T_2$ is the homogeneous linewidth. We expect $\alpha_2 > \alpha_1$ in the high-B_1 limit where $B_1 > B_{\mathrm{homog}}$.

Let us use eq. 56 as a starting point for developing an approximate $\boldsymbol{m}_z^{\mathrm{final}}$ expression that accounts for T_2 losses during the rapid passage. Developing this approximate expression is tricky because the Magnus expansion is not unconditionally convergent. The convergence

condition for the Magnus expansion is an ongoing area of research [61, 65–68]. The convergence condition is usually formulated for a quantum-mechanical system undergoing unitary evolution, with relaxation neglected. The usually-given convergence condition is [61]

$$\int_{-\tau_0}^{+\tau_0} \left\| \boldsymbol{B}_{\mathrm{eff}}^b(\tau) \right\|_2 d\tau < \pi,$$

(60)

with $\| \cdot \|_2$ shorthand for the 2-norm. At large integration times τ_0, the diagonal elements of the Ω_1 matrix become large and negative, violating the eq. 60 condition. However, in Ref. 67 it is noted that "one can easily construct examples showing that [eq. 60] is not necessary for the convergence of the expansion." It would appear that our eqs. 42 and 54 are one such example. At long time, $2\beta\tau_0 \gg 1$, the matrix Ω_1 is dominated by two large negative matrix elements at diagonal positions (1,1) and (2,2). In this limit, e^{Ω_1} is bounded, and the Magnus expansion is convergent by inspection.

In the absence of a clearly applicable convergence criterion, how to proceed? To guarantee convergence, we will be conservative and assume $2\beta\tau_0 \ll 1$, equivalent to requiring the total sweep time $2t_0$ to be much shorter than T_2, so that eq. 60 holds. At the same time, we would like to approximate the integrals in Ω_1 by their $a_0 \to \infty$ values. The integrands are of the form $1/(1 + a^2) \times$ oscillating function. We surmise that the integrals will be approximately converged for $\alpha_0 \gtrsim \pi$. This is equivalent to requiring $\alpha_2 \geq 1$, which guarantees that the α_2-related matrix elements in Ω_1 are suitably small. At very large α_2, however, eq. 56 reverts to eq. 49 and is uninteresting; we expect interesting behavior as α_2 decreases towards 1.

When $2\beta\tau_0 \ll 1, \alpha_2 \geq 1$, and $\alpha_2 \gg \alpha_1$, we find that Ω_1 is well approximated by

$$\Omega_1 \approx \begin{pmatrix} \dfrac{1}{2\alpha_2} & 0 & -\pi I_{13}(t_{\mathrm{sweep}}) \\ 0 & \dfrac{1}{2\alpha_2} & 0 \\ \pi I_{13}(t_{\mathrm{sweep}}) & 0 & -\dfrac{1}{\alpha_2} \end{pmatrix}.$$

(61)

When $\alpha_1 \ll 1$, the I_{13} terms are negligible and

$$m_z^{\mathrm{final}} \approx -e^{-1/\alpha_2} m_z^{\mathrm{initial}}.$$

(62)

In this limit, magnetization losses are small when $\alpha_2 \gg 1$. Mathematically, this limit is achieved when T_2 is large, B_1 is small, or the sweep is *fast*. To avoid T_2 losses, we need the magnetization to spend as little time as possible "near" the plane, where "near" means when

the resonance offset becomes comparable to B_1. This behavior is somewhat counterintuitive, because adiabatic losses are small when B_1 is large and the sweep is *slow*. We conclude that some compromise might be required to limit both T_2 and adiabatic losses during rapid passage. Considering eqs. 62 and 29, we propose

$$m_z^{\text{final}} = e^{-1/\alpha_2}\left(-1 + 2e^{-1/2\alpha_1}\right)m_z^{\text{initial}}$$

(63)

as an approximate expression that captures both T_2 and fast-sweep losses during rapid passage at high B_1.

3. Numerical simulations

Numerical simulations of magnetization versus time in a time-dependent offset experiment were carried out for the representative TEMPAMINE radical. Except where noted, the electron spin resonance parameters in Table 1 were used. Also shown in the table are useful reference fields: the saturation field B_{sat}, the critical Rabi frequency B_1^{crit}, and the homogeneous linewidth B_{homog}.

The Bloch equations were numerically integrated in Python. To facilitate numerical integration, the equations were put in the following homogeneous form [69]:

$$\frac{d}{dt}\boldsymbol{m}_4 = \boldsymbol{A}(t)\boldsymbol{m}_4$$

(64)

with

$$\boldsymbol{m}_4 = \left(M_x, M_y, M_z, M_{\text{eq}}\right)^T$$

(65)

an expanded 4-dimensional magnetization vector and

$$\boldsymbol{A}(t) = \begin{pmatrix} -r_2 & \gamma\Delta B_0(t) & 0 & 0 \\ -\gamma\Delta B_0(t) & -r_2 & \gamma B_1 & 0 \\ 0 & -\gamma B_1 & -r_1 & r_1 \\ 0 & 0 & 0 & 0 \end{pmatrix}$$

(66)

an expanded 4×4 Bloch matrix. In these equations M_{eq} is the equilibrium magnetization, $r_1 = 1/T_1$ is the spin-lattice relaxation rate, and $r_2 = 1/T_2$ is the spin dephasing rate. For numerical stability, time was expressed in units of μs, rates in units of μs^{-1}, and fields in units of mT.

When the resonance offset ΔB_0 is time-independent, eqs. 65 can be integrated to give $\boldsymbol{m}_4(t) = e^{t\boldsymbol{A}}\boldsymbol{m}_4(0)$. Implementing the matrix exponential using the `SciPy` package's `linalg.expm` function, we verified that direct integration of eqs. 65 gives an $\boldsymbol{m}_4(t)$ exhibiting the expected magnetization evolution and decay, including spin-lattice relaxation, following pulses applied both on and off resonance.

When the resonance offset is a function of time,

$$\Delta B_0(t) = (t - t_{\text{res}})\frac{d\Delta B_0}{dt},$$

(67)

with t_{res} the time at which resonance was reached and $d\Delta B_0/dt$ the field derivative. Simulations were run from time 0 to $2t_{\text{res}}$, with $2t_{\text{res}} \ll T_1$. In this case eqs. 65 were numerically integrated using the `scipy.integrate` module's `odeint` function to obtain $m_z(t)$.

3.1. Low-B B_1 simulations

To study the dependence of the final magnetization on α_1 in the low-B_1 regime, we fixed $B_1 = B_1^{\text{crit}} = 6.3\mu\text{T}$ and varied $d\Delta B_0/dt$. The Bloch equations were integrated with carefully chosen values of the sweep time t_{res} and sweep rate. The numerical integration became unstable at long time if the sweep rate was too large. If the final time was shortened to avoid this instability, then steady state was not reached. So the largest sweep rate could not be too large and the final time could not be too long.

With $t_{\text{res}} = 6\ \mu\text{s}$, we evolved magnetization with $d\Delta B_0/dt$ between $0.001\ \text{mT}\ \mu\text{s}^{-1}$ and $1\ \text{mT}\ \mu\text{s}^{-1}$; the associated α_1 values ranged from 4.54×10^{-2} to 4.54×10^{1}. Representative plots of $m_z(t)$ versus time t are shown in Fig. 2. From these plots a final magnetization was extracted as $m_s^{\text{final}} = m_z(12\ \mu\text{s})$ and plotted versus α_1.

3.2. High-B_1 simulations

To simulate magnetization dynamics in the high-B_1 regime, we set $d\Delta B_0/dt = 0.70\ \text{mT}\ \mu\text{s}^{-1}, t_{\text{res}} = 2\ \mu\text{s}$, and varied B_1 from $1.12\ \text{mT}$ to $3.56\ \mu\text{T}$; the associated α_1 values ranged from 1×10^{-3} to 1×10^{2}. As mentioned above, the simulation parameters were carefully chosen to meet the competing constraints of covering a five-order-of-magnitude variation in α_1, reaching steady-state, and avoiding long-time instability in the numerical integration of the Bloch equations.

Simulations were carried out for $T_2 = 0.45\ \mu\text{s}, 2.25\ \mu\text{s}$, and $13.5\ \mu\text{s}$. Representative plots of $m_z(t)$ versus time t are shown in Fig. 3 for the $T_2 = 2.25\ \mu s$ simulation. In contrast with the low-B_1 simulations of Fig. 2, large Rabi oscillations are now apparent. From such plots a final magnetization was extracted as $m_s^{\text{final}} = m_z(4\mu\text{s})$ and plotted versus α_1. To compare m_s^{final} to

theory, eqs. 56 and 63, we also need to know α_2. In an experiment in which B_1 is varied and $d\Delta B_0/dt$ is fixed, α_2 can be computed from α_1 as follows:

$$\alpha_2 = T_2\left(\frac{\alpha_1\gamma}{\pi}\frac{d\Delta B_0}{dt}\right)^{1/2}.$$

(68)

4. Experiments

Experimental studies of ^{1}H magnetization after an adiabatic rapid passage were carried out in a nuclear magnetic resonance experiment on polystyrene. The proton spins in polystyrene, like the unpaired electron spin in TEMPAMINE, have a T_1 and T_2 that differ by orders of magnitude [70, 71]. Atactic polystyrene (Sigma Aldrich, $\overline{M}_w = 211.6$k, lot no. 11326LH) was dissolved at 0.8% w/w in deuterated chloroform (Cambridge Isotopes, 99.8%, lot no. PR-33545/04142). No care was taken to remove dissolved oxygen from the solution. Liquid NMR experiments were performed at −60°C, slightly above the chloroform solvent freezing point, on a 500MHz Varian INOVA spectrometer equipped with an extended VT range Varian broadband probe; cooling the sample reduced T_2. Shaped pulses were generated with Pbox, as implemented in VnmrJ 2.2D, using a hard 90° pulse as a reference (14.9 μs at 57 dB coarse power). The longitudinal relaxation time T_1 was measured with the Varian Chempack inversion recovery sequence (INVREC; hard 180° and 90° pulses, 8 time points, 2 s acquisition time and 8 s repetition time). The transverse relaxation time T_2 was acquired with the Varian Chempack Carr-Purcell-Meiboom-Gill (CPMGT2) sequence; the echo time was 1 ms giving a 2 ms time resolution between positive echos.

The polystyrene NMR spectrum consists of ^{1}H resonances from aliphatic backbone protons (0.975 to 1.686 ppm and 1.778 to 2.289 ppm) and aromatic protons (ortho and meta at 6.031 to 6.913 ppm and para at 6.922 to 7.254 ppm). These resonances have distinct T_2 values. Equation 63 was tested by producing, using a modified Varian s2pul sequence, a fixed-amplitude linear frequency sweep "chirped" pulse followed by a $\pi/2$ pulse; the interpulse delay was 10 μs. The chirped pulse was between 25 and 100 ms long with a 47619 Hz sampling rate. For each measurement chirp B_1 was varied between 0.2 μT and 80 μT, corresponding to an α_1 sweep-rate parameter of 10^{-2} to 10^2. Data were processed with MNova 14.3.2 (Mestrelab Research). The T_1 and T_2 measurement integrals were fit in Python using the `lmfit` package.

5. Results and discussion

Simulation results are shown in Fig. 4, where they are compared to theory.

At low-B_1, Fig. 4(a), we see that saturation is effective for slow sweeps (*i.e.* small α_1) but becomes ineffective for fast sweeps (*i.e.* large α_1). Equation 25 quantitatively predicts the numerically calculated final magnetization over a three-order-of-magnitude variation in α_1.

At high-B_1, the final magnetization depends on α_1 in a more complicated way. Consider the $T_2 = 0.45$ μs simulation in Fig. 4(b). At large α_1, the irradiation is ineffective, as in the low-B_1 case. Now as α_1 is decreased, the magnetization becomes negative, indicating the onset of adiabatic inversion. Yet as α_1 is decreased further, adiabatic inversion fails, and the magnetization becomes merely saturated.

This counter-intuitive behavior can be understood as follows. During a suitably "slow" sweep (*i.e.* small α_1), the magnetization is effectively spin-locked along the direction of the effective field during an adiabatic passage through resonance. This situation corresponds to the magnetization remaining along the $\hat{z}_a$ axis in the tilted frame defined by T_a. According to eq. 37, the decay of the $\hat{z}_a$-axis magnetization is governed by the matrix element $(B_{\mathrm{eff}}^a)_{33}$. Writing out the differential equation governing this spin-locked magnetization $(m_a)_z$ in terms of time t,

$$\frac{d}{dt}(m_a)_z = -r_z^{\mathrm{a}}(m_a)_z$$

(69)

with

$$r_z^{\mathrm{a}} = \frac{1}{T_1}\frac{\Delta B_0(t)^2}{B_1^2 + \Delta B_0(t)^2} + \frac{1}{T_2}\frac{B_1^2}{B_1^2 + \Delta B_0(t)^2}$$

(70)

an effective relaxation rate. We see that the decay of spin-locked magnetization is T_1-like (*i.e.* slow) far away from resonance but is T_2-like (*i.e.* fast) near resonance. In the Fig. 4(b–d) simulations, B_1 is largest at small α_1. At low α_1, therefore, the magnetization spends a comparatively larger fraction of its evolution near resonance where T_2 losses are significant. The apparent reversion to saturation apparent at low α_1 in Fig. 4(b–d) is thus the result of a T_2-related loss of magnetization. Consistent with this explanation, at fixed α_1, these losses are smaller as T_2 is increased, as can be seen in Fig. 4(c) and Fig. 4(d).

At high B_1, we used two curves to describe the simulated magnetization in Fig. 4(b–d) — the empirical eq. 63 (solid line) and the first-order Magnus expansion, eq. 56, taken in the $2\beta\tau_0 \ll 1$, $a_0 \to \infty$ limit (dotted line). Of the two, eq. 63 describes the simulated magnetization better. Although we derived it rigorously, eq. 56 agrees only semiquantitatively with the LZSM result in the $T_2 \to \infty$ limit, so it is perhaps not surprising that this equation describes the magnetization imperfectly in the finite-T_2 limit as well. While our proposed semi-empirical eq. 63 was not derived rigorously, our Sec. 2 derivation shows why it is physically plausible.

Equation 63 was tested experimentally using ^{1}H spins in polystyrene dissolved in deuterated chloroform. The chemical structure and NMR spectrum of the polystyrene sample are shown in Fig. 5(top); four groups of protons are spectroscopically resolvable. The measured

relaxation times of the sample's protons are tabulated in Table 2. The T_1/T_2 ratio ranged from 41 for the group 1 aromatic protons to 241 for the group 4 aliphatic protons. Since $T_1/T_2 \gg 1$, the primary assumption underlying eq. 63 is valid for all groups of spins in the sample. For comparison, $T_1/T_2 = 2.8 \times 10^3$ for electron spins in TEMPAMINE.

The proton spectrum was acquired following an adiabatic rapid passage through all proton resonances in the sample. Rapid passages were carried out at a fixed sweep rate with B_1 varied. The final magnetization, normalized to the initial magnetization, was plotted versus α_1; see Fig. 5(bottom). The measured (colored squares), calculated (lines), and numerically computed (black circles) values of m_z^{final} are in good agreement. For all four groups of spins, eq. 63 correctly predicts (a) the failure to invert or even saturate magnetization at low B_1 (*i.e.* large α_1), (b) the existence of a maximally inverted magnetization at intermediate B_1 (at an α_1 value between 0.1 and 1), and (c) and a reversion to saturation at high B_1 (*i.e.* small α_1). The group 4, aliphatic spins follow eq. 63 quantitatively while spin groups 1 through 3 follow eq. 63 only qualitatively. This discrepancy cannot be due to the breakdown of the infinite-time approximation, *i.e.* $a_0 \to \infty$, because the numerical simulations (black circles) accounted for the finite sweep time. We surmise that the discrepancy is due to spins not behaving as isolated two-level systems, as our theory also assumes. The sweep time, 100 ms, is on the order of the inverse J coupling, so interference effects during the sweep could be a complicating factor.

6.   Conclusions

Our main findings are Eqs. 25 and 63, plotted against numerical simulations in Fig. 4. These simple analytical expressions for the final magnetization after a rapid passage through resonance, valid at low and high intensity, respectively, account for both the non-adiabatic and T_2 losses seen in exact numerical simulations over a wide range of irradiation intensities and field-sweep rates. Equation 63 was tested experimentally using nuclear spins and found to be in good agreement with experiment. The Appendix A method for numerically evaluating highly oscillatory integrals and the eq. 53 and 56 intermediate results are also noteworthy.

There is a large body of literature concerned with creating population inversions using adiabatic sweeps optimized for total power or operational bandwidth [10–18, 26, 27]. The most effective of these inversions employ sweeps in which *both* B_1 and the resonance offset ΔB_0 are time-dependent. Although we assumed above that B_1 was time-independent, it is straightforward to modify the definition of $\theta(\tau)$ in eqs. 35 and 36 to account for a time-dependent B_1. Our approach can thus be applied to account for non-adiabatic and T_2 losses in these more sophisticated inversion protocols.

Prior studies addressing relaxation in LZSM transitions have employed a wide range of methods: formal perturbation expansion series [23], a sum over paths [43], Bloch equations [44, 46, 54], Linblad equations [46, 50, 54], an imaginary Hamiltonian [52], master equations [54], and a two-level system coupled to a bath of bosons [45, 47–49, 51, 53, 55] or other two-level systems [47] (e.g. spin-boson models). The spin-boson models

generally include longitudinal (*i.e.* diagonal) bath couplings [49, 51, 55], to model T_2-like dephasing of coherence, and may also include transverse (*i.e.* off-diagonal) bath couplings [45, 47, 48, 53], to model T_1-like spin-lattice relaxation of population differences. Here we addressed relaxation in LZSM transitions using the Bloch equations, three coordinate transformations, and the Magnus expansion. There are only a few prior examples of using a Magnus expansion to treat LZSM transitions [33, 68], but these treatments neglected relaxation. Calculating the LZSM-transition probabilities in the dissipationless limit usually requires contour integration [34] or invoking opaque special-function solutions to a third-order differential equation [19]. It is therefore noteworthy that our relatively straightforward calculation reproduces semiquantitatively the well-known LZSM result (eq. 53, in the $T_2 \rightarrow \infty$ limit). Working in the $T_2 \ll T_1$ limit, it was easy to include T_2 losses using our approach. In contrast with nearly all prior work, we obtained closed-form expressions for the final population difference that depend explicitly on B_1 and T_2.

Our results agree with prior work. Some [23, 49], but not all [44], prior numerical studies of LZSM transitions including T_2 losses obtained behavior qualitatively similar to that seen in Fig. 4: the two-level system remains unperturbed at high sweep rate, imperfect adiabatic inversion is seen at intermediate sweep rate, and saturation is achieved at low sweep rate. Our low-B_1 result, eq. 25, reproduces eq. 15 in Ref. 72, derived via resumming a formal perturbation expansion series. Our high-B_1 result, eq. 63, has the same form as eq. 27 in Ref. 46, derived using an approach complimentary to ours.[1] The Ref. 46 derivation employed an interaction representation diagonalizing the Bloch matrix, assumed the nondissipative propagator is known, assumed (without justification) that the nondissipative propagator commutes with the dissipation matrix in both the adiabatic and non-adiabatic limits, and obtained corrections to the known LZSM dynamics arising from dissipation. In contrast, we have derived a T_2 correction to LZSM dynamics from first principles, eq. 56, having made no *ab initio* assumptions about the nondissipative propagator.

Nevertheless, we make a number of uncontrolled approximations, and further work is needed to make our derivation more rigorous. The first such assumption requires $2\beta\tau_0 \ll 1$. This condition seems unnecessarily conservative given (1) the obvious convergence of the Magnus expansion at long times, as discussed following eq. 60, and (2) the good agreement between eq. 63, numerical calculations, and experiments at times $2\beta\tau_0 \gg 1$. To go beyond the $2\beta\tau_0 \ll 1$ requirement we need a Magnus-expansion convergence criterion applicable to the sort of real matrices considered here — a significant undertaking. The second uncontrolled approximation is computing the eq. 56 integrals only in the $a_0 \rightarrow \infty$, infinite-time limit. We have not been able to generalize the Appendix A integration scheme to finite a_0; the integrals at finite a_0 can be computed numerically but this approach is prohibitively slow. The agreement between eq. 63, numerical Bloch-equation simulations, and experiments indicates that the eq. 56 integrals are close to their $a_0 \rightarrow \infty$ limit for the large-bandwidth, finite-time sweeps considered here.

---

[1]We caution that the exponential factor in the Ref. 46, eq. 15 formula contains a typographical error. In Ref. 46, the exponential factor η in Table I, the Landau-Zener sweep case, is given by $\eta = \pi\Gamma\Omega_0 T$, which has incorrect units Reproducing the last steps in the Ref. 46 derivation of the exponential factor, we obtain $\eta = \pi\Gamma\Omega_0 T^2$, equal to $1/\alpha_2$ in our notation.

Finally, we can use our results to design magnetic resonance force microscope experiments. Consider an experiment [73] employing a radius $a = 50$ nm cobalt sphere (saturation magnetization $\mu_0 M_s = 1.8$ T) operating at a tip-sample separation of $h = 30$ nm. The sphere is magnetized along the z direction and oscillates in the x direction, moving parallel to a sample surface. To compute the time-dependent magnetic field experienced by the sample, it is helpful to know the tip field gradient [74]

$$\frac{dB_z^{\text{tip}}}{dx} = -\frac{a^3 \mu_0 M_s}{2r^4}(3 + 5\cos 2\theta)\sin\theta\cos\phi$$

(71)

where we have expressed the gradient in polar coordinates, with θ defined relative to z, ϕ defined relative to x, and r the radial distance relative to the center of the sphere. The gradient is zero directly beneath the tip. The gradient is maximized along the $x = 0$ line (*i.e.* $\phi = 0$) at an angle $\theta_{\text{opt}} \approx 0.175\pi$. At that location, using $r = a + h$,

$$\frac{dB_z^{\text{tip}}}{dx} = -1.377\frac{\mu_0 M_s a^3}{(a+h)^4}$$

(72)

The spherical magnet is attached to a cantilever whose position is time dependent: $x(t) = x_{0p}\cos(2\pi f_0 t)$, with $x_{0p} = 164$ nm the zero-to-peak cantilever amplitude and $f_0 = 7.3$ kHz the cantilever oscillation frequency. The peak time-dependent field experienced by a spin at angle θ_{opt} and tip-sample separation h is

$$\frac{d\Delta B_0}{dt} = \frac{dB_z^{\text{tip}}}{dx}\frac{dx}{dt} = -8.652\frac{f_0 \mu_0 M_s a^3 x_{0p}}{(a+h)^4} = 5.69 \times 10^4 \text{ T s}^{-1}$$

(73)

where we have evaluated dx/dt at the zero crossing where the derivative is maximum.

In the presence of the eq. 73 field sweep, eq. 21 tells us that achieving $\alpha_1 \leq 1$ requires $B_1 \geq 320\mu$T. One would naively think that to saturate the electron spin magnetization would require $B_1 \approx 10B_{\text{sat}} = 2.4$ μT. The above analysis shows that, surprisingly, an irradiation intensity B_1 more than 10^2-fold larger than $10B_{\text{sat}}$ is actually required to fully saturate the electron spin in the presence of the moving tip.

Supplementary Material

Refer to Web version on PubMed Central for supplementary material.
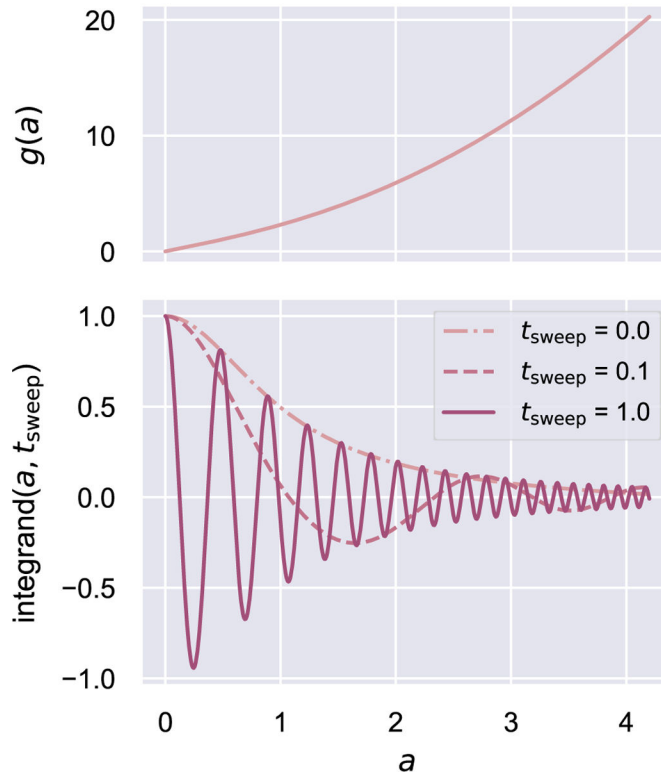
Acknowledgments

Appendix A.: Numerically integrating a highly oscillatory function

We wish to evaluate the integral

$$I_{13}(t_{\text{sweep}}) = \int_{-\infty}^{\infty} \frac{1}{\pi} \frac{\cos(2\pi t_{\text{sweep}} g(a))}{1 + a^2} da$$

(A.1)

with

$$g(a) = a\sqrt{1 + a^2} + \text{arcsinh}(a)$$

(A.2)

Figure A.6:

The Eq. A.1 integrand is highly oscillatory. (a) The Eq. A.2 function $g(a)$ versus a. (b) The Eq. A.1 integrand for various values of the parameter t.

and

$$t_{sweep} = \frac{1}{(2\pi)^2 \alpha_1}$$

(A.3)

an inverse sweep-rate parameter. Other integrals of interest are

$$I_{11}(t_{sweep}) = \int_{-\infty}^{\infty} \frac{1}{\pi} \frac{\cos(4\pi t_{sweep} g(a))}{1 + a^2} da = I_{13}(2t_{sweep})$$

(A.4)

and

$$I_{23}(t_{sweep}) = \int_{-\infty}^{\infty} \frac{1}{\pi} \frac{a \sin(2\pi t_{sweep} g(a))}{1 + a^2} da.$$

(A.5)

The function $g(a)$ is plotted in Fig. A.6(a). The Eq. A.1 integrand is plotted in Fig. A.6(b) for selected values of the parameter t. For large values of a, the integration variable, $g(a) \sim a^2$. The Eq. A.1 integrand is highly oscillatory, with the oscillation frequency continuously increasing. This is true of the Eq. A.4 and A.5 integrands as well.

Computing the Eq. A.1 integral using standard integration packages is problematic and slow, especially when t is large. When $t_{sweep} = 0$, $I(0) = 1$. Another useful reference value is $t_{sweep,ref} = 0.0466475$. *Mathematica* returns $I(t_{sweep,ref}) = 0.5000$ without error in 85 ms. *Mathematica* is advertised as handling a wide range of one-dimensional and multidimensional integrals. Yet for $t \geq 2.2$, *Mathematica* returns the error `NIntegrate failed to converge`.

Computing $I(t_{sweep,ref})$ using the Python function `scipy.integrate.quad()` returns 0.4925 ± 0.0036 in 35 ms with the message `IntegrationWarning: The maximum number of subdivisions (50) has been achieved`. Increasing the number of subdivisions to `limit = 5000` returns $0.500028 \pm 2.2 \times 10^{-5}$, but the integration requires 2.2 s and still returns an `IntegrationWarning` error.

The Python function `mpmath.quadosc()` is specifically optimized to integrate oscillating functions. The function performs the Eq. A.1 integral well, provided it is fed an asymptotic formula for the integrand's zeros. Evaluating $I(t_{sweep,ref})$ using mpmath.quadosc () and integrating over the $[0, \infty]$ interval with the argument `zeros=lambda n:mp.sqrt(mp.pi*n/0.0466475)` returns 0.50000046 without error, but takes 2.5 s to do so. In our application, we need many thousands of integral evaluations. These evaluations require over 30 min using `mpmath.quadosc()`. We clearly need a faster way to evaluate integrals like Eq. A.1.

To carry out the above integrals, we adapted an inverse-function approach suggested by Evans [75, 76]. Let h be the inverse function of g. That is

$$h(g(a)) = a$$

(A.6a)

$$g(a) \equiv b$$

(A.6b)

$$a = h(b)$$

(A.6c)

Substituting Eq. A.6b into Eq. A.1 and changing the integration variable from a to b using Eq. A.6c transforms Eq. A.1 to

$$I_{13}(t_{\text{sweep}}) = \int_{-\infty}^{\infty} \frac{1}{\pi} \frac{\cos(2\pi t_{\text{sweep}} b)}{1 + h(b)^2} \frac{dh}{db} db.$$

(A.7)

By changing the integration variable, we have removed the variable-frequency oscillation from the integrand. However, at this point neither h nor dh/db is known. We can actually derive a formula for dh/db, as follows. Substituting Eqs. A.6b and A.6c into Eq. A.2 we obtain

$$b = h(b)\sqrt{1 + h(b)^2} + \text{arcsinh}\,(h(b)).$$

(A.8)

Differentiating both sides of this equation with respect to b yields an implicit equation for dh/db, which may be solved to obtain

$$\frac{dh}{db} = \frac{1}{2\sqrt{1 + h(b)^2}}.$$

(A.9)

Substituting this result into Eq. A.7 gives

$$I_{13}(t_{\text{sweep}}) = \int_{-\infty}^{\infty} \frac{1}{\pi} \frac{\cos(2\pi t_{\text{sweep}} b)}{\left(1 + h(b)^2\right)^{3/2}} db.$$

(A.10)

According to Eq. A.10, the integral $I(t_{\text{sweep}})$ and the function $1/\left(1 + h(b)^2\right)^{3/2}$ are Fourier transform pairs. We can therefore compute I at an array of t_{sweep} values rapidly using the fast Fourier transform (FFT) algorithm.

It remains to determine the inverse function $h(b)$. Given the complicated form of $g(a)$, Eq. A.2, there is unfortunately no analytic formula for the inverse function h. Given a set of b_j values, however, we can determine values of the inverse function h_j *numerically* using an iterative algorithm, as follows.

Suppose we have a good guess for the inverse function. At large a, $g(a) \approx a^2$, which suggests $h_{\text{approx}}(b) = \sqrt{b}$ as an approximate inverse function. Applied to b_0, the approximate inverse function yields $h_0 = h_{\text{approx}}(b_0)$. If we have guessed the inverse function well, then $g(h_0)$ will be close to b_0. Employing a Taylor series, let us write

$$b_0 = g(h_0 + \delta h_0) \approx g(h_0) + g'(h_0)\delta h_0$$

(A.11)

where δh_0 is an error we can use to improve our estimate of the inverse function and $g'(a) = dg/da = 2\sqrt{1 + a^2}$. Solving for δh_0,

$$\delta h_0 \approx \frac{b_0 - g(h_0)}{g'(h_0)}$$

(A.12)

We can create an updated estimate of the inverse function using

$$h_1 = h_0 + \epsilon \delta h_0$$

(A.13)

with $\epsilon \leq 1$ a convergence factor. We can apply Eqs. A.12 and A.13 iteratively to obtain a converged estimate of the value of the inverse function at b_0. While the algorithm was just described for a single b value, it can be carried out on an entire array of values simultaneously.

Representative results are shown in Fig. A.7. An array of 5×10^5 b values was created and the above algorithm was run for 75 iterations with $\epsilon = 0.25$, taking 2 s. The resulting inverse function is plotted in Fig. A.7(a). As an accuracy check, we can apply the original function g to the inverse function $h(b)$. The result should be $g(h(b)) = b$, a line with zero intercept and unit slope; this is observed, Fig. A.7(b). The relative error, $(g(h(b)) - b)/b$, is plotted in Fig. A.7(c) with the $b = 0$ point removed to avoid a division-by-zero error. The relative error is worst at small b, but is no larger than approximately 10^{-7} after as few as 75 iterations.

From the resulting $h_j = h(b_j)$ values we computed an array $1/(1 + h_j^2)^{3/2}$; $I_j = I_{13}(t_{\text{sweep},j})$ values were computed from this array via FFT. Some thought is required to perform the FFT. The variables b and t_{sweep} are Fourier transform pairs, with b and t_{sweep} playing the role of frequency and time, respectively. Recall that $t_{\text{sweep}} = 1/(2\pi)^2\alpha_1$. We are interested in computing the integral for α_1 values ranging from $\alpha_1^{\text{max}} = 10^2$ to $\alpha_1^{\text{min}} = 10^{-3}$, corresponding to t_{sweep} values ranging from

$$t_{\text{sweep}}^{\text{min}} = 1/(2\pi)^2\alpha_1^{\text{max}} = 2.53 \times 10^{-4}$$
$$t_{\text{sweep}}^{\text{max}} = 1/(2\pi)^2\alpha_1^{\text{min}} = 2.53 \times 10^1 .$$

We created an array of $N_{t_{\text{sweep}}} = 2^{17} = 131072$ $t_{\text{sweep},j}$ values using $t_{\text{sweep}}^{\text{min}}$ as the time step. Working in Python, the `np.fft.fftfreq` function was used to create an array of negative and positive b_j values from the $t_{\text{sweep},j}$ values. We created an array of inverse function values h_j using the above algorithm and implemented the Eq. A.10 integral, using the `np.fft.ifft` function to obtain an array of I_j values. Because of the even symmetry of the h_j values, the resulting I_j values are artificially symmetric; only $t_{\text{sweep},j}$ values with indices $\left[0, N_{t_{\text{sweep}}}/2\right]$ are meaningful.

The I_{11} and I_{23} integrals were computed analogously. The resulting integrals are plotted versus t_{sweep} in Fig. A.8.
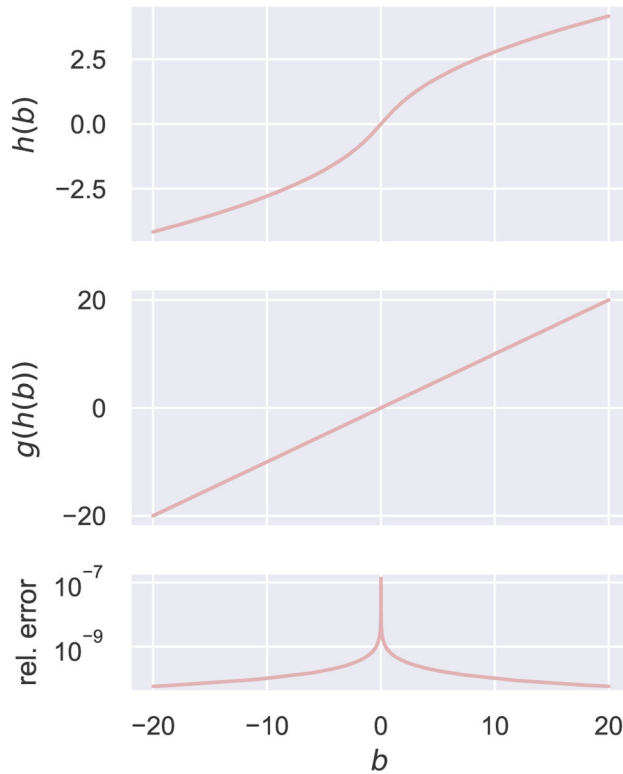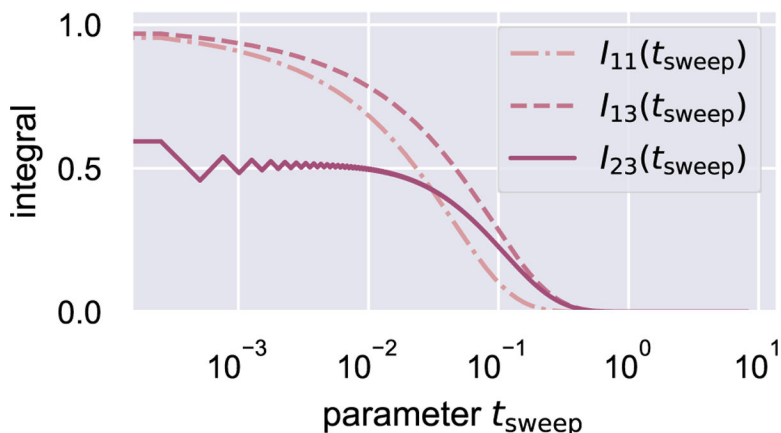

Figure A.7:

Iterative determination of the inverse function $h(b)$, Eq. A.6, using the algorithm described in the text. Upper: The resulting inverse function. Middle: An accuracy check. Bottom: The relative error.

Selected values of the integral were compared to `mpmath.quadosc()` results. The fractional error in I_{13} was as large as 1.4×10^{-2} at $t_{sweep} = 0$ where $I_{13} = 1$, improved to 7.2×10^{-4} at t_{sweep}^{min} where $I_{13} = 0.5$, and deceased further at larger t_{sweep} values. The associated error in magnetization at $t_{sweep} = 0$ is nevertheless only 1.0×10^{-3} because $\cos(\pi I_{13})$ is a quadratic function near $I_{13} = 1$. The evaluation of the integral by the inverse-function/FFT method took only 0.5 s for 131072 points, compared to an extrapolated 80 h for the same number of points using `mpmath.quadosc()`.

To create Fig. 1, a final magnetization, m_z^{final}, was computed from the I_{13} integral and plotted versus the array $\alpha_1 = 1/(2\pi)^2 t_{sweep}$, with the $t_{sweep} = 0$ point discarded.

Figure A.8:
The integrals $I_{13}(t_{sweep})$, $I_{11}(t_{sweep})$, and $I_{23}(t_{sweep})$ versus t_{sweep}. Note the logarithmic x axis (the $t_{sweep} = 0$ point has been discarded). The integral was computed numerically using the inverse-function/FFT method described in the text. Declaration of Interest Statement (docx format)

References

[1]. Köhler J, Disselhorst JAJM, Donckers MCJM, Groenen EJJ, Schmidt J, Moerner WE, Magnetic resonance of a single molecular spin, Nature 363 (1993) 242–244. doi:10.1038/363242a0.

[2]. Wrachtrup J, von Borczyskowski C, Bernard J, Orrit M, Brown R, Optical-detection of magnetic-resonance in a single molecule, Nature 363 (1993) 244–245. doi:10.1038/363244a0.

[3]. Rugar D, Budakian R, Mamin HJ, Chui BW, Single spin detection by magnetic resonance force microscopy, Nature 430 (2004) 329–332. doi:10.1038/nature02658. [PubMed: 15254532]

[4]. Grinolds MS, Hong S, Maletinsky P, Luan L, Lukin MD, Walsworth RL, Yacoby A, Nanoscale magnetic imaging of a single electron spin under ambient conditions, Nat. Phys 9 (2013) 215–219. doi:10/f4szjx.

[5]. Grinolds MS, Warner M, De Greve K, Dovzhenko Y, Thiel L, Walsworth RL, Hong S, Maletinsky P, Yacoby A, Subnanometre resolution in three-dimensional magnetic resonance imaging of individual dark spins, Nat. Nanotech 9 (2014) 279–284. doi:10.1038/nnano.2014.30.

[6]. Yacoby A, Personal communication, 2015.

[7]. Moore EW, Lee S-G, Hickman SA, Wright SJ, Harrell LE, Borbat PP, Freed JH, Marohn JA, Scanned-probe detection of electron spin resonance from a nitroxide spin probe, Proc. Natl. Acad. Sci. U.S.A 106 (2009) 22251–22256. doi:10.1073/pnas.0908120106. [PubMed: 20018707]

[8]. Nguyen HL, Marohn JA, Reverse Monte Carlo reconstruction of electron spin-label coordinates from scanned-probe magnetic resonance microscope signals, arXiv:1802.07247 (2018). arXiv: 1802 .07247.

[9]. Garner SR, Kuehn S, Dawlaty JM, Jenkins NE, Marohn JA, Force-gradient detected nuclear magnetic resonance, Appl. Phys. Lett 84 (2004) 5091–5093. doi:10.1063/1.1762700.

[10]. Silver MS, Joseph RI, Hoult DI, Selective spin inversion in nuclear magnetic resonance and coherent optics through an exact solution of the Bloch-Riccati equation, Phys. Rev. A 31 (1985) 2753–2755. doi:10.1103/PhysRevA.31.2753.

[11]. Baum J, Tycko R, Pines A, Broadband and adiabatic inversion of a two-level system by phase-modulated pulses, Phys. Rev. A 32 (1985) 3435–3447. doi:10.1103/PhysRevA.32.3435.

[12]. Kupce E, Freeman R, Adiabatic pulses for wideband inversion and broadband decoupling, J. Magn. Reson., Ser. A 115 (1995) 273–276. doi:10.1006/jmra.1995.1179.

[13]. Kupce E, Freeman R, Stretched adiabatic pulses for broadband spin inversion, J. Magn. Reson., Ser. A 117 (1995) 246–256. doi:10.1006/jmra.1995.0750.

[14]. Tannús A, Garwood M, Improved performance of frequency-swept pulses using offset-independent adiabaticity, Journal of Magnetic Resonance, Series A 120 (1996) 133–137. doi:10.1006/jmra.1996.0110.

[15]. Tannús A, Garwood M, Adiabatic pulses, NMR Biomed. 10 (1997) 423–434. doi:10.1002/(SICI)1099-1492(199712)10:8<423:AID-NBM488>3.0.C0;2-X. [PubMed: 9542739]

[16]. Garwood M, DelaBarre L, The return of the frequency sweep: Designing adiabatic pulses for contemporary NMR, J. Magn. Reson 153 (2001) 155–177. doi:10.1006/jmre.2001.2340. [PubMed: 11740891]

[17]. Doll A, Jeschke G, Wideband frequency-swept excitation in pulsed EPR spectroscopy, J. Magn. Reson 280 (2017) 46–62. doi:10.1016/j.jmr.2017.01.004. [PubMed: 28579102]

[18]. Gan Z, An analytical treatment of electron spectral saturation for dynamic nuclear polarization NMR of rotating solids, J. Chem. Phys 158 (2023) 024114. doi:10.1063/5.0109077. [PubMed: 36641384]

[19]. Ivakhnenko OV, Shevchenko SN, Nori F, Nonadiabatic Landau–Zener–Stückelberg–Majorana transitions, dynamics, and interference, Physics Reports 995 (2023) 1–89. doi:10.1016/j.physrep.2022.10.002.

[20]. Rosen N, Zener C, Double Stern-Gerlach experiment and related collision phenomena, Phys. Rev 40 (1932) 502–507. doi:10.1103/PhysRev.40.502.

[21]. Frauenfelder H, Wolynes PG, Rate theories and puzzles of hemeprotein kinetics, Science 229 (1985) 337–345. doi:10.1126/science.4012322. [PubMed: 4012322]

[22]. Garg A, Onuchic JN, Ambegaokar V, Effect of friction on electron transfer in biomolecules, J. Chem. Phys 83 (1985) 4491–4503. doi:10.1063/1.449017.

[23]. Kayanuma Y, Population inversion in optical adiabatic rapid passage with phase relaxation, Phys. Rev. Lett 58 (1987) 1934–1936. doi:10.1103/PhysRevLett.58.1934. [PubMed: 10034576]

[24]. Economou SE, Sham LJ, Wu Y, Steel DG, Proposal for optical U(1) rotations of electron spin trapped in a quantum dot, Phys. Rev. B 74 (2006) 205415. doi:10.1103/PhysRevB.74.205415.

[25]. Poem E, Kenneth O, Kodriano Y, Benny Y, Khatsevich S, Avron JE, Gershoni D, Optically induced rotation of an exciton spin in a semiconductor quantum dot, Phys. Rev. Lett 107 (2011) 087401. doi:10.1103/PhysRevLett.107.087401. [PubMed: 21929205]

[26]. Barnes E, Das Sarma S, Analytically solvable driven time-dependent two-level quantum systems, Phys. Rev. Lett 109 (2012) 060401. doi:10.1103/PhysRevLett.109.060401. [PubMed: 23006253]

[27]. Barnes E, Analytically solvable two-level quantum systems and Landau-Zener interferometry, Phys. Rev. A 88 (2013) 013818. doi:10.1103/PhysRevA.88.013818.

[28]. Grimaudo R, Vitanov NV, Messina A, Coupling-assisted Landau-Majorana-Stückelberg-Zener transition in a system of two interacting spin qubits, Phys. Rev. B 99 (2019) 174416. doi:10.1103/PhysRevB.99.174416.

Author Manuscript

Author Manuscript

Author Manuscript

Author Manuscript

[29]. Grimaudo R, Nakazato H, Messina A, Vitanov NV, Dzyaloshinskii-Moriya and dipole-dipole interactions affect coupling-based Landau-Majorana-Stückelberg-Zener transitions, Phys. Rev. Res 2 (2020) 033092. doi:10.1103/PhysRevResearch.2.033092.

[30]. Grimaudo R, Vitanov NV, Messina A, Landau-Majorana-Stückelberg-Zener dynamics driven by coupling for two interacting qutrit systems, Phys. Rev. B 99 (2019) 214406. doi:10.1103/PhysRevB.99.214406.

[31]. Militello B, Three-state Landau-Zener model in the presence of dissipation, Phys. Rev. A 99 (2019) 033415. doi:10.1103/PhysRevA.99.033415.

[32]. Militello B, Detuning-induced robustness of a three-state Landau-Zener model against dissipation, Phys. Rev. A 99 (2019) 063412. doi:10.1103/PhysRevA.99.063412.

[33]. Munoz-Bauza H, Chen H, Lidar D, A double-slit proposal for quantum annealing, npj Quantum Inf 5 (2019) 1–11. doi:10.1038/s41534-019-0160-0.

[34]. Wittig C, The Landau–Zener formula J. Phys. Chem. B 109 (2005) 8428–8430. doi:10.1021/jp040627u. [PubMed: 16851989]

[35]. Michaeli S, Sorce DJ, Idiyatullin D, Ugurbil K, Garwood M, Transverse relaxation in the rotating frame induced by chemical exchange, Journal of Magnetic Resonance 169 (2004) 293–299. doi:10.1016/j.jmr.2004.05.010. [PubMed: 15261625]

[36]. Sorce DJ, Michaeli S, Garwood M, The time-dependence of exchange-induced relaxation during modulated radio frequency pulses, Journal of Magnetic Resonance 179 (2006) 136–139. doi:10.1016/j.jmr.2005.11.001. [PubMed: 16298149]

[37]. Michaeli S, Sorce DJ, Springer CS, Ugurbil K, Garwood M, $t_1\rho$ MRI contrast in the human brain: Modulation of the longitudinal rotating frame relaxation shutter-speed during an adiabatic RF pulse, Journal of Magnetic Resonance 181 (2006) 135–147. doi:10.1016/j.jmr.2006.04.002. [PubMed: 16675277]

[38]. Mangia S, Liimatainen T, Garwood M, Michaeli S, Rotating frame relaxation during adiabatic pulses vs. conventional spin lock: simulations and experimental results at 4 T, Magn. Reson. Imaging 27 (2009) 1074–1087. doi:10.1016/j.mri.2009.05.023. [PubMed: 19559559]

[39]. Mangia S, Traaseth NJ, Veglia G, Garwood M, Michaeli S, Probing slow protein dynamics by adiabatic $r_1\rho$ and $r_{2\rho}$ NMR experiments, J. Am. Chem. Soc 132 (2010) 9979–9981. doi:10.1021/ja1038787. [PubMed: 20590094]

[40]. Traaseth NJ, Chao F-A, Masterson LR, Mangia S, Garwood M, Michaeli S, Seelig B, Veglia G, Heteronuclear adiabatic relaxation dispersion ({HARD}) for quantitative analysis of conformational dynamics in proteins, Journal of Magnetic Resonance 219 (2012) 75–82. doi:10.1016/j.jmr.2012.03.024. [PubMed: 22621977]

[41]. Barbara TM, Nonadiabatic exchange dynamics during adiabatic frequency sweeps, Journal of Magnetic Resonance 265 (2016) 45–51. doi:10.1016/j.jmr.2016.01.017 [PubMed: 26852417]

[42]. Chao F-A, Byrd RA, Geometric approximation: A new computational approach to characterize protein dynamics from nmr adiabatic relaxation dispersion experiments, J. Am. Chem. Soc 138 (2016) 7337–7345. doi:10.1021/jacs.6b02786. [PubMed: 27225523]

[43]. Shimshoni E, Stern A, Dephasing of interference in Landau-Zener transitions, Phys. Rev. B 47 (1993) 9523–9536. doi:10.1103/PhysRevB.47.9523.

[44]. Ivanov PA, Vitanov NV, Adiabatic evolution amidst dephasing, Phys. Rev. A 71 (2005) 063407. doi:10.1103/PhysRevA.71.063407.

[45]. Wubs M, Saito K, Kohler S, Hänggi P, Kayanuma Y, Gauging a quantum heat bath with dissipative Landau-Zener transitions, Phys. Rev. Lett 97 (2006) 200404. doi:10.1103/PhysRevLett.97.200404. [PubMed: 17155667]

[46]. Lacour X, Guérin S, Yatsenko LP, Vitanov NV, Jauslin HR, Uniform analytic description of dephasing effects in two-state transitions, Phys. Rev. A 75 (2007) 033417. doi:10.1103/PhysRevA.75.033417.

[47]. Saito K, Wubs M, Kohler S, Kayanuma Y, Hänggi P, Dissipative Landau-Zener transitions of a qubit: Bathspecific and universal behavior, Phys. Rev. B 75 (2007) 214308. doi:10.1103/PhysRevB.75.214308.

[48]. Pokrovsky VL, Sun D, Fast quantum noise in the Landau-Zener transition, Phys. Rev. B 76 (2007) 024310. doi:10.1103/PhysRevB.76.024310.

[49]. Nalbach P, Thorwart M, Landau-Zener transitions in a dissipative environment: Numerically exact results, Phys. Rev. Lett 103 (2009) 220401. doi:10.1103/PhysRevLett.103.220401. [PubMed: 20366076]

[50]. Avron JE, Fraas M, Graf GM, Grech P, Landau-Zener tunneling for dephasing Lindblad evolutions, Commun. Math. Phys 305 (2011) 633–639. doi:10.1007/s00220-011-1269-y.

[51]. Orth PP, Imambekov A, Le Hur K, Nonperturbative stochastic method for driven spin-boson model, Phys. Rev. B 87 (2013) 014305. doi:10.1103/PhysRevB.87.014305.

[52]. Avishai Y, Band YB, Landau-Zener problem with decay and dephasing, Phys. Rev. A 90 (2014) 032116. doi:10.1103/PhysRevA.90.032116.

[53]. Xu C, Poudel A, Vavilov MG, Nonadiabatic dynamics of a slowly driven dissipative two-level system, Phys Rev. A 89 (2014) 052102. doi:10.1103/PhysRevA.89.052102.

[54]. Zlatanov KN, Vasilev GS, Ivanov PA, Vitanov NV, Exact solution of the Bloch equations for the nonresonant exponential model in the presence of dephasing, Phys. Rev. A 92 (2015) 043404. doi:10.1103/PhysRevA.92.043404.

[55]. Zhuang F, Zeng J, Economou SE, Barnes E, Noise-resistant Landau-Zener sweeps from geometrical curves, Quantum 6 (2022) 639. doi:10.22331/q-2022-02-02-639.

[56]. Bloch F, Nuclear induction, Phys. Rev 70 (1946) 460–474. doi:10.1103/PhysRev.70.460.

[57]. Torrey HC, Transient nutations in nuclear magnetic resonance, Phys. Rev 76 (1949) 1059–1068. doi:10.1103/PhysRev.76.1059.

[58]. Feynman RP, Vernon FL, Hellwarth RW, Geometrical representation of the Schrödinger equation for solving maser problems, J. Appl. Phys 28 (1957) 49–52. doi:10.1063/1.1722572.

[59]. Madhu PK, Kumar A, Bloch equations revisited: New analytical solutions for the generalized Bloch equations, Concepts Magn. Reson 9 (1997) 1–12. doi:10.1002/(sici)1099-0534(1997)9:1<1::aid-cmr1>3.0.co;2-2.

[60]. Magnus W, On the exponential solution of differential equations for a linear operator, Comm. Pure Appl. Math 7 (1954) 649–673. doi:10.1002/cpa.3160070404.

[61]. Blanes S, Casas F, Oteo J, Ros J, The Magnus expansion and some of its applications, Phys. Rep 470 (2009) 151–238. doi: 10.1016/j.physrep.2008.11.001.

[62]. Klein O, Naletov V, Alloul H, Mechanical detection of nuclear spin relaxation in a micron-size crystal, Eur. Phys. J. B 17 (2000) 57–68. doi:10.1007/s100510070160.

[63]. Harrell LE, Thurber KR, Smith DD, Cantilever noise in off-cantilever-resonance force-detected nuclear magnetic resonance, J. Appl. Phys 95 (2004) 2577–2581. doi:10.1063/1.1643780.

[64]. Rubbmark JR, Kash MM, Littman MG, Kleppner D, Dynamical effects at avoided level crossings: A study of the Landau-Zener effect using Rydberg atoms, Phys. Rev. A 23 (1981) 3107–3117. doi:10.1103/PhysRevA.23.3107.

[65]. Fel'dman EB, On the convergence of the Magnus expansion for spin systems in periodic magnetic fields, Phys Lett. A 104 (1984) 479–481. doi:10.1016/0375-9601(84)90027-6.

[66]. Moan PC, Oteo JA, Convergence of the exponential Lie series, J. Math. Phys 42 (2001) 501–508. doi:10.1063/1.1330198.

[67]. Casas F, Sufficient conditions for the convergence of the Magnus expansion, J. Phys. A: Math. Theor 40 (2007) 15001. doi:10.1088/1751-8113/40/50/006.

[68]. Begzjav TK, Eleuch H, Magnus expansion applied to a dissipative driven two-level system, Results in Physics 17 (2020) 103098. doi:10.1016/j.rinp.2020.103098.

[69]. Bain AD, Anand CK, Nie Z, Exact solution to the Bloch equations and application to the Hahn echo, J. Magn. Reson 206 (2010) 227–240. doi:10.1016/j.jmr.2010.07.012. [PubMed: 20692859]

[70]. Lauprêtre F, Noël C, Monnerie L, Dynamics of macromolecular chains. {VI}. carbon {13} and proton nuclear magnetic relaxation of polystyrene in solution, J. Polym. Sci. Polym. Phys. Ed 15 (1977) 2127–2142. doi:10.1002/pol.1977.180151208.

[71]. Heatley F, Nuclear magnetic relaxation of synthetic polymers in dilute solution, Prog. Nucl. Magn. Reson. Spectrosc 13 (1979) 47–85. doi:10.1016/0079-6565(79)80013-8.

[72]. Kayanuma Y, Phase coherence and nonadiabatic transition at a level crossing in a periodically driven two-leve system, Phys. Rev. B 47 (1993) 9940–9943. doi:10.1103/PhysRevB.47.9940.

[73]. Boucher MC, Isaac CE, Sun P, Borbat PP, Marohn JA, A non-perturbative, low-noise surface coating for sensitive force-gradient detection of electron spin resonance in thin films, ACS Nano 17 (2023) 1153–1165. doi:10.1021/acsnano.2c08635.

[74]. Kempf JG, Marohn JA, Nanoscale fourier-transform imaging with magnetic resonance force microscopy, Phys. Rev. Lett 90 (2003) 087601. doi:10.1103/PhysRevLett.90.087601. [PubMed: 12633459]

[75]. Evans GA, An alternative method for irregular oscillatory integrals over a finite range, Int. J. Comput. Math 52 (1994) 185–193. doi:10.1080/00207169408804303.

[76]. Evans GA, Webster JR, A comparison of some methods for the evaluation of highly oscillatory integrals, J. Comput. Appl. Math 112 (1999) 55–69. doi:10.1016/S0377-0427(99)00213-7.

Revised Highlights

- Accounting for dephasing losses during rapid-passage experiments is challenging

- Treat with Bloch equations, coordinate transformations, and a Magnus expansion

- Obtain analytic equations accounting for both adiabaticity and T_2 dephasing losses

- Need a larger B_1 than expected in electron-spin magnetic resonance force microscopy

- A compromise B_1 may be required to limit T_2 and adiabatic losses during passage
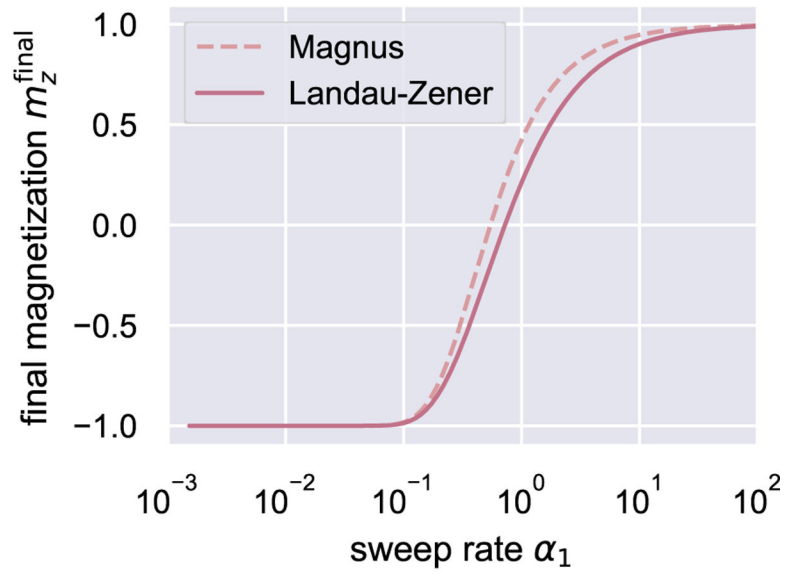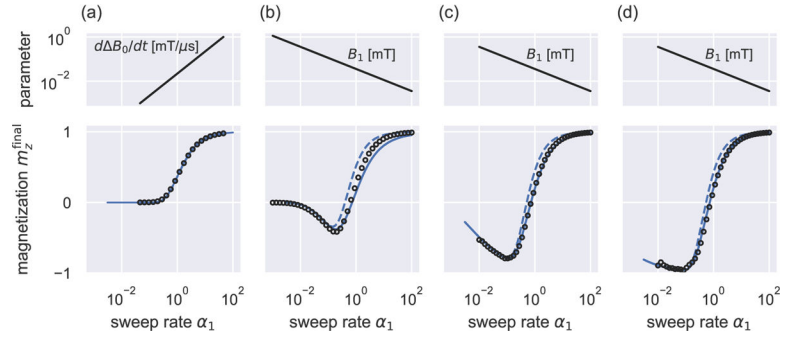
Figure 1:
Final magnetization versus the unitless sweep-rate parameter. The final magnetization was computed, neglecting relaxation, using the Magnus expansion (dotted line, eq. 53) and the LZSM formula (solid line, eq. 29).
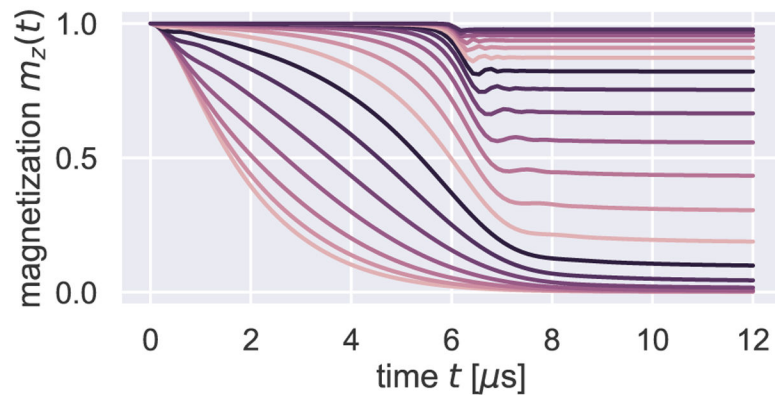
Figure 2:
Calculated magnetization versus time in the low-B_1 regime. Simulation details: resonance parameters from Table 1; field intensity $B_1 = 6.3\ \mu$T; and, from bottom to top, 20 different sweep rates $d\Delta B_0/dt$ logarithmically distributed between 0.001 mT μs^{-1} (bottom) to 1 mT μs^{-1} (top).
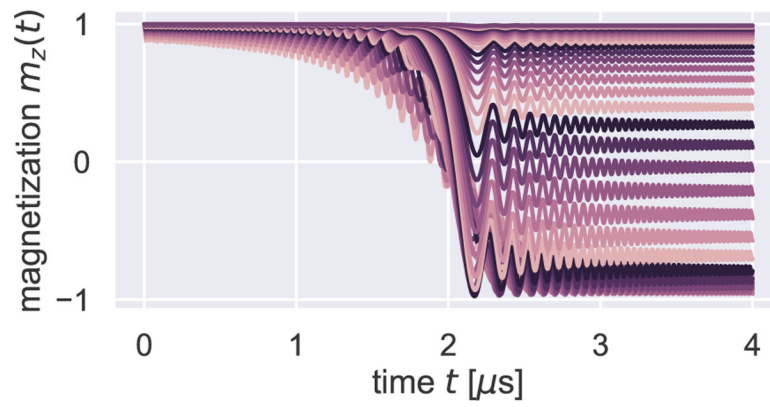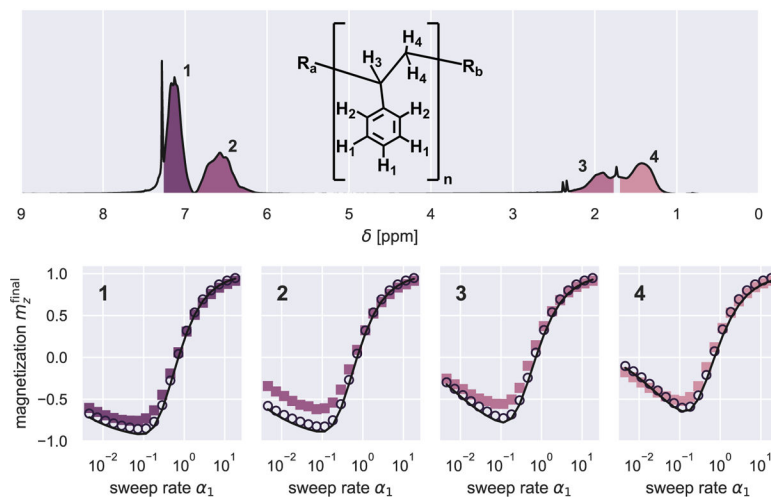
Figure 3:
Calculated magnetization versus time in the high-B_1 regime. Simulation details: resonance parameters from Table 1, except $T_2 = 2.25$ μs sweep rate $d \, \Delta B_0/dt = 0.70$ mT μs^{-1} and, from bottom to top, 40 different B_1 values logarithmically distributed between 1.12 mT (bottom) to 3.56 μT (top).

Figure 4:
Simulated final magnetization m_z^{final}, after a sweep through resonance, plotted versus the unitless sweep rate α_1. The Bloch equations were numerically integrated at (a) low intensity ($B_1 = 6.3\ \mu$T, $T_2 = 0.45\ \mu$s, and variable $d\Delta B_0/dt$) and at (b-d) high intensity ($d\Delta B_0/dt = 0.70$ mT μs^{-1}, variable B_1, and T_2 equal to (b) $0.45\ \mu$s, (c) $2.25\ \mu$s, and (d) $13.5\ \mu$s). In the top plots we graph the varied parameter, $d\Delta B_0/dt$ in (a) and B_1 in (b-d), versus α_1, while on the bottom plots we graph the final magnetization. Open circles are the numerically computed magnetization. In (a), the solid line is eq. 25. In (b-d), the solid line is eq. 63 while the dotted line is the magnetization computed using the first-order Magnus expansion in eq. 56 taken in the $2\beta\tau_0 \ll 1$, $a_0 \rightarrow \infty$ limit.

Figure 5:
Experimental measurement of final magnetization after a sweep through resonance. Top: Solution ^{1}H NMR of 200k polystyrene in CDCl$_3$ at -60°C and 500 MHz. The integrated NMR peaks used in the analysis are numbered and shaded in purple. Bottom: Final magnetization after a chirped pulse plotted vs. the α_1 sweep-rate parameter for the four numbered resonances (sweep rate = 800 kHz s^{-1}, sweep time $2t_0 = 100$ ms). Colored squares are experimental data, black circles are numerical simulations, and black lines are eq. 63.

Table 1:

Electron spin resonance parameters for TEMPAMINE.

variable	definition	numerical value
γ		$2\pi \times 28.0\,\mathrm{GHz\,T^{-1}}$
T_2	$1/r_2$	$0.45\ \mu\mathrm{s}$
T_1	$1/r_1$	1.3 ms
B_{sat}	$1/\left(\gamma\sqrt{T_1 T_2}\right)$	$0.24\ \mu\mathrm{T}$
B_1^{crit}	$(r_2 - r_1)/(2\gamma)$	$6.3\ \mu\mathrm{T}$
B_{homog}	$1/(\gamma T_2)$	$12.6\ \mu\mathrm{T}$

Table 2:

Relaxation times of polystyrene in deuterated chloroform at −60 °C and 500 MHz.

spin	T_1[ms]	T_2[ms]	T_1/T_2
1	1430 (10)	35.1 (0.6)	41
2	1393 (04)	24.5 (0.2)	57
3	1400 (10)	10.4 (0.2)	135
4	1370 (20)	5.6 (0.2)	241